

TRIS. I. ABSOLUTE MEASUREMENTS OF THE SKY BRIGHTNESS TEMPERATURE AT 0.6, 0.82, AND 2.5 GHz

M. ZANNONI,¹ A. TARTARI, M. GERVASI,^{1,2} G. BOELLA,² G. SIRONI,¹ A. DE LUCIA, AND A. PASSERINI
 Physics Department, University of Milano Bicocca, I20126 Milan, Italy; mario.zannoni@mib.infn.it

AND

F. CAVALIERE
 Physics Department, University of Milano, I20133 Milan, Italy
 Received 2007 October 3; accepted 2008 June 5

ABSTRACT

At frequencies close to 1 GHz the sky diffuse radiation is a superposition of radiation of Galactic origin, the 3 K relic or cosmic microwave background radiation, and the signal produced by unresolved extragalactic sources. Because of their different origin and space distribution, the relative importance of the three components varies with frequency and depends on the direction of observation. With the aim of disentangling the components we built TRIS, a system of three radiometers, and studied the temperature of the sky at $\nu = 0.6, 0.82,$ and 2.5 GHz using geometrically scaled antennas with identical beams (HPBW = $18^\circ \times 23^\circ$). Observations included drift scans along a circle at constant declination $\delta = +42^\circ$, which provided the dependence of the sky signal on the right ascension, and absolute measurement of the sky temperature at selected points along the same scan circle. TRIS was installed at Campo Imperatore (latitude = $42^\circ 26'$ north, longitude = $13^\circ 33'$, elevation = 2000 m a.s.l.) in central Italy, close to the Gran Sasso Laboratory.

Subject headings: cosmic microwave background — diffuse radiation — instrumentation: miscellaneous — radio continuum: galaxies — radio continuum: ISM

1. INTRODUCTION

The diffuse radiation from the sky is a superposition of components. At frequencies between few tens of MHz and few tens of GHz, in terms of brightness temperature we can write

$$T_{\text{sky}}(\alpha, \delta, \nu) = T_{\text{Gal}}(\alpha, \delta, \nu) + T_{\text{CMB}}(\nu) + T_{\text{UERS}}(\nu), \quad (1)$$

where α and δ are the right ascension and declination, respectively, of the point at which the telescope axis is aimed. T_{Gal} is the Galactic contribution: partially polarized, anisotropically distributed, it tracks the Galactic structure. Its frequency spectrum is a power law

$$T_{\text{Gal}}(\nu, \alpha, \delta) = K(\alpha, \delta)\nu^{-\beta(\alpha, \delta)}, \quad (2)$$

with spectral index β ranging from 2.1 to 3.4 depending on the relative weight of thermal and synchrotron emission, on the energy spectrum of the cosmic-ray electrons, and on the galactic magnetic field. Compared to the other components of the diffuse radiation, it is a foreground and dominates the sky at frequencies below ~ 1 GHz.

T_{CMB} is the cosmic microwave background. Relic of the big bang, it is substantially unpolarized and isotropically distributed. Its flat frequency spectrum is consistent with the emission of a blackbody with a temperature of 2.725 ± 0.001 K (Fixsen & Mather 2002). Compared to the other components, it is a true background. At $\nu \geq 1$ GHz T_{CMB} definitely overcomes T_{Gal} and dominates the sky up to $\nu \sim 100$ GHz, above which thermal emis-

sions from an irregular distribution of dust with physical temperature ≥ 20 K gradually overwhelm the other components.

T_{UERS} is a blend of unresolved extragalactic radio sources isotropically distributed. Its frequency spectrum is a power law

$$T_{\text{UERS}} = K_{\text{UERS}}\nu^{-\gamma_{\text{UERS}}}, \quad (3)$$

with $\gamma_{\text{UERS}} \sim 2.70$ (Gervasi et al. 2008a).

Each of the above components carries important astrophysical and/or cosmological information, particularly at decimetric wavelengths. At these frequencies, for instance, we can expect a dip in the flat spectrum of T_{CMB} , whose detection can provide direct information on Ω_b (Burigana et al. 1991), the universe baryon density. In this same region the slope of the power-law frequency spectrum of T_{Gal} changes, revealing perhaps a knee in the energy spectrum of the cosmic-ray electrons responsible for the Galactic synchrotron radiation. To disentangle these components, coordinated, multifrequency observations of extended areas of sky are necessary. They will form a database from which the desired information can be extracted modeling the components and optimizing the model parameters. At frequencies close to 1 GHz it is possible to find in literature maps of T_{sky} that cover all the sky or large parts of it (see Table 1). Their accuracy is, however, insufficient to answer many of the questions put forth by present-day astrophysical and cosmological models. These maps have been in fact obtained combining data collected at different sites and/or at different times and frequently show artificial structures, e.g., *stripes*. Once *destriped* (see, e.g., Platania et al. 2003), these maps can be used to extract the spectral index of the Galactic signal T_{Gal} . The accuracy of the zero level of the absolute scale of temperature of the same maps is, however, still insufficient to disentangle the radiation components with the accuracy today required by cosmology. To overcome this difficulty, we made absolute and differential measurements of the diffuse radiation at three frequencies,

¹ Also Italian National Institute for Astrophysics, INAF, Milan, Italy.

² Also Italian National Institute for Nuclear Physics, INFN, Milano-Bicocca, Italy.

TABLE 1
EXTENDED MAPS OF THE DIFFUSE RADIATION

ν (GHz)	δT_{zero} (K)	δT (%)	Angular Resolution (deg)	Sky Coverage	References
0.022.....	$\simeq 10^3$...	1.1×1.7	North	1
0.038.....	300	5	7.5	North	2
0.151.....	40	$\simeq 10$	5	Full	3
0.408.....	3	$\simeq 10$	0.85	Full	4
0.820.....	0.6	$\simeq 10$	1.2	North	5
1.420.....	0.5	$\simeq 10$	0.6	North	6
2.326.....	0.08	≤ 5	0.33	South	7

REFERENCES.—(1) Roger et al. 1999; (2) Milogradov-Turin & Smith 1973; (3) Landecker & Wielebinsky 1970; (4) Haslam et al. 1982; (5) Berkhuijsen 1972; (6) Reich & Reich 1986; (7) Jonas et al. 1998.

using a set of three radiometers (therefore the project is called TRIS), at 0.6, 0.82, and 2.5 GHz. In this paper we present results of these observations. In Gervasi et al. (2008b, hereafter Paper II) and Tartari et al. (2008, hereafter Paper III), the astrophysical and cosmological implications of TRIS data are discussed.

2. ABSOLUTE MEASUREMENTS OF TEMPERATURE

Measuring the absolute value of the *brightness temperature*, T_{sky} , of a patch of diffuse radiation is a conceptually simple but not easy task. Large systematic effects are in fact expected.

A radiometer aimed at the sky gives the *antenna temperature*, T_a , from which we obtain

$$T_{\text{sky}} = \frac{T_a - T_{\text{atm}} - T_{\text{env}}}{1 - (T_{\text{atm}}/T_{\text{atm}}^0)}, \quad (4)$$

where T_{atm} and T_{env} are the noise temperatures of the signals from the atmosphere and the environment, respectively, above and around the radiometer and $T_{\text{atm}}^0 \simeq 240$ K is the physical temperature of the atmosphere (Committee on Extensions to the Standard Atmosphere 1976). References for calculations are presented in § 4.3.1. Since the diffuse radiation fills the antenna beam, the absolute value of T_a is

$$T_a = T_{\text{cold}}^{\text{eff}} + (S_{\text{sky}} - S_{\text{cold}})G, \quad (5)$$

where

$$G = \frac{T_{\text{warm}}^{\text{eff}} - T_{\text{cold}}^{\text{eff}}}{S_{\text{warm}} - S_{\text{cold}}} \quad (6)$$

is the system *gain* or *conversion factor* and S_{sky} , S_{cold} , and S_{warm} are the radiometer outputs produced by the sky target and by two known sources (*calibrators*), a *cold* and a *warm* load. T_x^{eff} , the *effective temperature* of calibrator x , is the convolution of the calibrator brightness temperature and the antenna beam pattern. Effects of antenna and receiver properties (gain, bandwidth, physical temperature, and attenuation of the components between the antenna mouth and the radiometer output) are included in G .

With one important exception (Stankevich et al. 1970) astronomical objects have been rarely used as absolute calibrators. In fact, unless the source is isolated, it completely fills the antenna beam, and its brightness distribution is precisely known, the accuracies of T_x^{eff} , G , and T_a are poor. Artificial blackbodies, shaped to fit the antenna aperture, to match the antenna impedance, and to fill the antenna beam, are more convenient calibrators because their effective and brightness temperatures coincide. They have

TABLE 2
TYPICAL ACCURACY OF MEASURED VALUES
OF T_{sky} IN LITERATURE

ν_0 (GHz)	σ (mK)
100–60.....	1–10
60–10.....	10–50
10–1.....	10–500
1–0.5.....	500–1500

been used (Bensadoun et al. 1992) at frequencies $\nu > 1$ GHz ($\lambda < 30$ cm) where the radiation wavelength, the antenna aperture $A_e = \lambda^2/\Omega_a$ (Ω_a is the antenna solid angle), and the blackbody dimensions are reasonably small. Small dimensions make it also possible to bring the radiometer in space (e.g., Mather et al. 1994) or at balloon altitudes (e.g., Kogut et al. 2006) where atmospheric and environmental effects are negligible or absent and $T_a \simeq T_{\text{sky}}$ (see § 4.3.1 and eq. [12]).

Below 1 GHz, however, the antenna dimensions and the wavelength are large and discourage the construction of artificial sources that fit the antenna mouth and fill the antenna beam. Moreover, at these low frequencies observations from space or at balloon altitudes are extremely difficult and calibrations are better made injecting at some point between antenna and receiver, through a multi-throw switch, the noise produced by very compact line terminations (the so-called dummy loads) properly cooled or warmed.

In this case the effective temperature of the calibrator is

$$T_l^{\text{eff}} = \left[T_l^0 e^{-\tau_c} + \int_0^L T_c^0(x) e^{-\tau(x)} \left(\frac{d\tau}{dx} \right) dx \right] (1 - r^2) + r^2 T_{\text{RX}}^{\text{eff}}, \quad (7)$$

where T_l^0 and $T_c^0(x)$ are the physical temperatures of the load and the transmission line *connecting* the load to the switch, respectively, x is a coordinate running on the line, $d\tau/dx$ is the specific attenuation (neper per unit length) of the line, $e^{-\tau_c}$ is the transmission of the line, r^2 is the power reflection coefficient of the load seen through the line, and $T_{\text{RX}}^{\text{eff}}$ is the noise temperature radiated by the receiver (see § 3.4).

Usually the accuracy of G is good but T_a , being measured at the switch positions, must be corrected (see, e.g., eq. [11]) for the transmission $e^{-\tau_{\text{LC}}}$ and *thermal noise*

$$T_{\text{noise}} = \int_0^{\tau_{\text{LC}}} T_0(x) e^{-\tau(x)} d\tau = \bar{T}_0 (1 - e^{-\tau_{\text{LC}}}) \quad (8)$$

of the lossy components (LCs) at temperature T_0 distributed along the line between the switch and the antenna mouth. To limit the statistical and systematic uncertainties on T_{noise} , the temperature of these components must be low and stable. In fact, equation (8) gives

$$(\delta T_{\text{noise}})^2 \simeq (T_0 \delta \tau_{\text{LC}})^2 + (\tau_{\text{LC}} \delta T_0)^2 \quad (\tau_{\text{LC}} \ll 1), \quad (9)$$

e.g., $0.3 \text{ K} \leq \delta T_{\text{noise}} \leq 3 \text{ K}$ if $T_0 \simeq 300 \text{ K}$ and $10^{-3} \leq \tau_{\text{LC}} \leq 10^{-2}$. For the above reasons the values of T_{sky} measured at frequencies close to and below 1 GHz have been so far less accurate than the values measured at higher frequencies.

Reviews in the literature (see, e.g., Sironi et al. 1999; Zannoni et al. 1999; Salvaterra & Burigana 2002; see also Table 2) show that below 10 GHz the accuracy of T_{sky} rapidly decreases with frequency

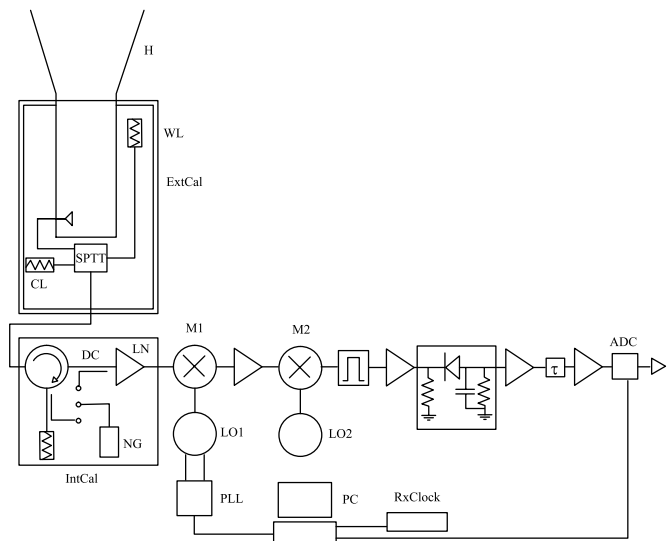


FIG. 1.—Block diagram of TRIS Radiometers. H = corrugated horn; LN = low-noise amplifier; LO1, LO2 = local oscillators; M1, M2 = mixers; PLL = phase-locked loop; τ = system time constant; ADC = analog-to-digital converter; PC = personal computer; RxClock = radio clock; ExtCal = external calibrator (WL = warm load; CL = cold load; SPTT = switch); IntCal = internal calibrator (C = circulator; DC = directional coupler; NG = noise generator).

and it is very poor below 1 GHz. Moreover, between 1 and 0.5 GHz the large dispersion of the error bars assigned by different observers to their results suggests that sometimes in the past not all the systematic effects were recognized. The frequency dependence of the accuracy of T_{sky} is especially evident in coordinated experiments like the multifrequency observations made by the White Mountain Collaboration (Smoot et al. 1985), the South Pole Collaboration (Bersanelli et al. 1993), and by ARCADE (Kogut et al. 2004). These experiments cover the frequency interval 2–100 GHz and approach the frequency region close to 1 GHz where neither T_{CMB} nor T_{Gal} is dominant and the models of T_{Gal} and T_{UERS} are insufficient to extract with the desired accuracy the cosmological signal. Additional observations at even lower frequencies were subsequently made at 1.4, 0.82, and 0.61 GHz (Bensadoun et al. 1993; Sironi et al. 1990, 1991). Unfortunately, those last observations used different systems and were not coordinated among them, nor with previous observations at the same or at higher frequencies. TRIS has been planned to carry on coordinated observations between 0.6 and 2.5 GHz with the aim of improving the accuracy of the existing data.

3. TRIS

TRIS is a set of three absolute radiometers that operate in total power configuration. All the radiometers have the same antenna

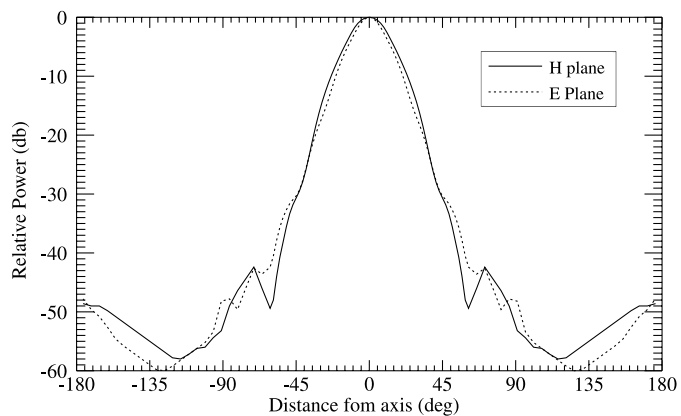


FIG. 2.—Beam of TRIS antennas measured on a geometrically scaled model at 8.2 GHz (solid line: H-plane; dotted line: E-plane).

beam, similar receivers, and include an External Calibrator unit and an Internal Calibrator unit (see Fig. 1).

The frequencies of operation (0.6 GHz [$\lambda = 50$ cm], 0.82 GHz [$\lambda = 36$ cm], and 2.5 GHz [$\lambda = 12$ cm]) were chosen because they span a frequency region where the ratio $T_{\text{Gal}}/T_{\text{CMB}}$ is >1 at low frequencies and <1 at high frequencies and because they were used in the past for similar observations.

3.1. Antennas

To have the same beam, the three antennas are geometrically scaled (i.e., their linear dimensions are the same in wavelength units). We chose pyramidal rectangular horns with corrugated (thin corrugations) E-plane walls and a corrugated E-plane corona at the mouth (see Table 3) because they have measurable and/or calculable electromagnetic properties. These antennas have a beam solid angle Ω_a wide enough to dilute the contribution of isolated sources well below the signal produced by the diffuse radiation but capable to keep track of the main features of the radiation spatial distribution. Side and back lobes are low (≤ -30 dB; Fig. 2) to minimize spillover from the ground and interferences. The electromagnetic signal is extracted from the antenna through a tunable (five tuning stubs) coaxial-waveguide transition. A prototype of the complete antenna at 8.2 GHz was built and tested in an anechoic chamber. Then the 2.5 GHz was made scaling the 8.2 GHz unit and optimizing the waveguide-coaxial transition. The 0.6 and 0.82 GHz horns were then scaled from it. Horn walls, corrugations, corona, waveguide sections, and waveguide-coaxial transition are made of anticorrosional riveted plates. These parts are fastened with screws for easy disassembling and transportation (before going to Campo Imperatore the 0.82 and 2.5 GHz horns were used at the Amundsen Scott base at the South Pole). Aluminum tape on all the joints provides optimum electrical contacts among the various

TABLE 3
TRIS ANTENNAS

Parameter	$\nu_0 = 0.60$ GHz	$\nu_0 = 0.82$ GHz	$\nu_0 = 2.5$ GHz
Horn aperture	$3.7\lambda \times 4.9\lambda$	$3.7\lambda \times 4.9\lambda$	$3.7\lambda \times 4.9\lambda$
Flare angle E-plane (deg)	19	19	19
Flare angle H-plane (deg)	23	23	23
Phase difference δ_E	0.07λ	0.07λ	0.07λ
Phase difference δ_H	0.10λ	0.10λ	0.10λ
HPBW (deg)	18 (E) \times 23 (H)	18 (E) \times 23 (H)	18 (E) \times 23 (H)
Mouth dimensions (m)	1.85×2.41	1.35×1.79	0.44×0.59
Horn length (m)	2.50	1.83	0.60
Back lobes (dB)	< -40	< -40	< -40

TABLE 4
TRANSMISSION $e^{-\tau}$ OF THE TRIS FRONT-END COMPONENTS

Component ^a	$\nu = 0.6$ GHz	$\nu = 0.82$ GHz	$\nu = 2.5$ GHz
WG cable (cold)	0.957 ± 0.001	0.9698 ± 0.0004	0.969 ± 0.006
WG cable (warm)	0.9600 ± 0.0001	...
WG transition.....	0.988 ± 0.002	0.986 ± 0.004	0.984 ± 0.004
WG3-1.....	0.9981 ± 0.0003	0.9966 ± 0.0002	0.997 ± 0.002
Wind-1.....	>0.99999	>0.99999	>0.99998
WG3-2.....	0.9983 ± 0.0003	0.9965 ± 0.0002	0.998 ± 0.001
Wind-2.....	>0.99998	>0.99998	>0.99998
WG2.....	0.9989 ± 0.0002	0.9997 ± 0.0002	0.9995 ± 0.0003
WG1.....	0.9983 ± 0.0001	0.9991 ± 0.0001	0.9985 ± 0.0001
WG ex.....	0.9978 ± 0.0002
Horn.....	0.9920 ± 0.0001	0.9872 ± 0.0001	0.9972 ± 0.0001

^a See text and Fig. 4.

parts and makes them insensitive to variable weather conditions and oxidation.

The 0.6, 0.82, and 2.5 GHz units were too large for the available anechoic chambers. The horn beam was therefore measured on the 8.2 GHz prototype in an anechoic chamber and at a test range, putting special care on side and back lobes. Results, presented in Figure 2, give a beam solid angle of 18° (E) \times 23° (H) (HPBW). Tests on the 0.6, 0.82, and 2.5 GHz units, made looking at the transit of the Sun, confirmed it.

The transmission $e^{-\tau}$ of the components that bring the signals from the antenna throat to the receiver was measured at 0.6, 0.82, and 2.5 GHz with a Vector Network Analyzer (Agilent 8510C) in laboratory. The attenuations of the horn between mouth and throat were calculated. Results are shown in Table 4.

At Campo Imperatore the three antennas were on an almost east-west row, on stands that allow us to steer the beam along the E-plane. This plane is titled 7° from the north-south plane in direction N \rightarrow NE and S \rightarrow SW. This plane crosses the southern profile of the surrounding mountains at azimuth 187° , where there is a brief leveling (see Fig. 3).

3.2. External Calibrator

A single pole triple throw (SPTT) switch is used to link the receiver to the antenna, the cold calibrator, or the warm calibrator. The switch is a source of thermal noise. The maximum accuracy one can reach in evaluating it is set by the repeatability of the switch attenuation and by the stability of its temperature (see eqs. [8] and [9]). To minimize this noise and its fluctuations, the

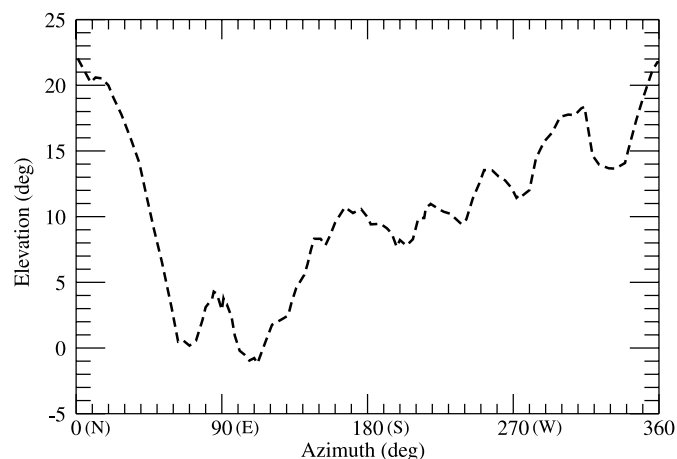


FIG. 3.—Horizon profile at Campo Imperatore.

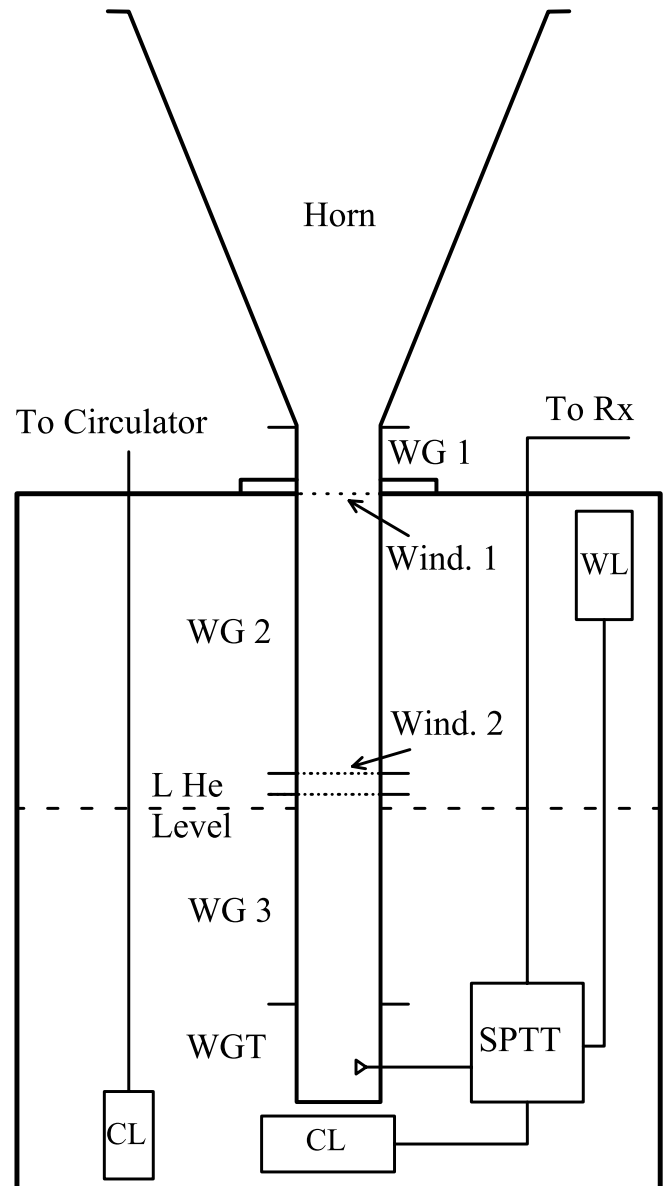


FIG. 4.—Schematic view of the cryogenic external calibrator (WG 1 = anti-corodal waveguide section; WG 2, WG 3 = stainless steel waveguide sections; Wind. 1 = polyethylene window; Wind. 2 = fluorglass windows; WGT = brass coaxial-waveguide transition; SPTT = single pole triple throw switch; WL = warm dummy load; CL = cold dummy load; see also Table 4 and text).

switch is cooled at temperatures comparable to the sky temperature and is stabilized putting it in a bath of liquid helium. Because no commercially available units satisfied our needs, we studied and built a cryogenic, purely passive, manually driven, resonant coaxial SPTT switch based on $\lambda/4$ lines (Zannoni et al. 1999). With $\tau \leq 0.01$ dB and $\delta\tau \leq 2.3 \times 10^{-3}$ it gives $\delta T_{\text{noise,switch}} \leq 10$ mK when cooled at 3.967 K, the boiling temperature of liquid helium at Campo Imperatore (2000 m a.s.l.). When cooled the switch can be driven through fiber glass rods that come out from the dewar housing it.

3.2.1. Cryogenic Waveguide

To minimize their thermal noise, all the lossy components distributed between the horn throat and the receiver input are cooled. The cryogenic SPTT switch, the waveguide-coaxial transition, and two 50Ω dummy loads are mounted at the bottom of a dewar (see Fig. 4), where they are always plunged in liquid helium (LHe).

TABLE 5
TRIS RECEIVER

Parameter	$\nu_0 = 0.60$ GHz	$\nu_0 = 0.82$ GHz	$\nu_0 = 2.5$ GHz
Tunability frequency range (MHz)	20	20	200
Number of selectable frequencies	256	256	256
Integration bandwidth (MHz)	0.3	0.3	3.0
Sampling time (s)	4	4	4
Noise temperature (K)	120	120	100
T_{RX}^{eff} (K)	84.5	67.3	72.6
T_{cold}^{eff} (K)	4.1	4.3	7.1
T_{warm}^{eff} (K)	231.4	247.2	247.1
Gain (10^{-4} K div $^{-1}$)	8.498 ± 0.004	7.130 ± 0.001	7.234 ± 0.001

^a Typical values (helium level dependent).

The third load is at the top of the dewar, at a stable temperature close to the external ambient temperature. A special stainless steel waveguide section brings the electromagnetic signal from the waveguide transition to the dewar top where it can be attached to the horn throat.

The stainless steel guide section is a thermal insulator. A window made of a polyethylene sheet in the collar at the top of the stainless steel section and two fluorglass (a special fabric transparent to radio and microwaves, opaque to IR) sheets in the stainless steel waveguide limit the input of thermal radiation. Holes in the fluorglass windows allow a uniform distribution of the cold helium vapors inside the waveguide.

A cable that goes through the flange at the dewar mouth links one of the two cold dummy loads to the circulator third port in the Internal Calibration Unit (see Fig. 1). A second cable links the switch output to the receiver input. The three inputs of the switch go to (1) the antenna coaxial input through a very short piece of cable at LHe temperature, (2) the second cold dummy load (the *cold source*), and (3) the load at the top of the dewar (the *warm load*) through a long cable. Sensors monitor the level of the liquid helium and the temperatures of switch, cold and warm loads, waveguide walls, and cables inside and outside the dewar.

A 250 liter dewar can house the 0.6 GHz or the 0.82 GHz system. It is sufficient to carry on observations for more than 48 hr without refilling. The 2.5 GHz system is in a 100 liter dewar. Once filled with helium, it allows continuous observation for about 90 hr.

The effective temperatures of the cold loads are larger than 3.967 K, the boiling temperature of LHe at the observing site, because of the unavoidable electromagnetic mismatches that carry in a fraction of the noise temperature radiated by the receiver (see eq. [7] and Table 5). Their values, however, can be calculated. The high value of T_{cl}^{eff} at 2.5 GHz is a consequence of the increasing difficulties of matching resonant systems when the wavelength decreases. The complete structure of the horn and cryogenic waveguide is shown in Figure 4.

3.2.2. Warm Waveguide

A more simple calibrator based on a small dewar containing just the SPTT switch and the three dummy loads was also prepared. It requires a limited quantity of LHe. It was used for preliminary tests and for 0.82 GHz absolute measurements when the dewar of the cryogenic waveguide failed. The final accuracy one gets on T_{sky} is, however, worse compared to the accuracy one gets using the cryogenic waveguide because of the noise produced by the lossy components, including the waveguide-coaxial transition, at ambient temperature.

3.3. Internal Calibrator and Reflectometer

A combination of circulators, directional couplers, solid-state noise source, matched dummy loads, and electrically driven switches form a unit, mounted between the receiver input and the low-noise amplifier (see Fig. 1; IntCal block). It can be used for the following:

1. To check the electromagnetic matching of the components attached at the receiver input. This is done turning on the solid-state noise source and sending its signal toward the receiver input. The measured variations of the receiver outputs ΔO_{inj} and ΔO_{ref} , when the receiver input is, respectively, short circuited or connected to the device under test, give the *power reflection coefficient* $r^2 = \Delta O_{ref}/\Delta O_{inj}$ (*reflectometer mode*).
2. To check the receiver gain sending the noise generator signal into the receiver (*internal calibration mode*).
3. To set to a known level the effective temperature T_{RX}^{eff} of the noise the receiver radiates toward the antenna. This is the *effective noise temperature* T_N^{eff} of the load at the third port of the circulator (see eq. [7] and Fig. 1). When this load is cooled at liquid helium temperature (see below), T_{RX}^{eff} can be of few tens of kelvins.

The internal calibrator and the reflectometer are used for regular checks of the radiometer performance during the observations. Cross-checks are made on site with a scalar network analyzer.

3.4. Receivers

TRIS receivers are standard heterodyne chains with double frequency conversion, total gain of ~ 100 dB, used in total power configuration (see Fig. 1 and Table 5). The frequency of the local oscillator LO1 can be adjusted digitally (see Fig. 1) so one can tune the observing channel among 256 adjacent frequencies separated by $\Delta\nu$, symmetrically distributed around the system nominal frequency ν_0 . $\Delta\nu$ is 75 kHz at 0.6 and 0.82 GHz, spanning a range of 20 MHz, and 750 kHz at 2.5 GHz, over a range of 200 MHz. The integration bandwidth is 0.3 MHz at 0.60 and 0.82 GHz and 3 MHz at 2.5 GHz.

The postdetection integration time constant is 10 s. After integration the receiver output is sampled and digitally converted every 4 s. Each sampled value, the housekeeping data, and the time signal are written in a record and stored on the hard disk of the personal computer that drives the local oscillator LO1. The time signals arrive from a master clock locked to radio signals regularly transmitted by I.E.N. Galileo Ferraris in Turin. The same clock drives the computer clock and guides the observational sequence. To avoid digital noise, the 20 bit AD converter is integrated into the detector channel and data are transmitted via optocoupler to the data recording system.

Measurements in total power configuration can be affected by gain instabilities. To compensate for them, the receiver detection channel includes zero-bias Schottky diodes and temperature stabilization of the DC section (active control with accuracy better than 0.1°C). The receiver temperature is set at stable values ($\pm 0.1^\circ\text{C}$) chosen between 25°C and 35°C for excursions of the external temperature from well below zero up to the preset value (usually $+35^\circ\text{C}$). Gain variations can be monitored and, when necessary, recovered looking at the amplitude of the internal calibrator signal (see below). They are usually small ($\leq 2\%$) except in rare occasions during observations around the local noon when clear sky and no breeze may bring the external temperature of the receiver box above the preset value. When this situation occurs, data are rejected.

4. OBSERVATIONS

Between 1990 and 1993 prototypes of the three radiometers and antennas were installed at Campo Imperatore (latitude = $42^\circ 26'$ north, longitude = $13^\circ 33'$ east), a plateau 2000 m a.s.l. The site is reasonably shielded against unwanted signals from the horizon by a circle of low-elevation mountains (see Fig. 3). Served by road in summer and by cable car in winter, the site is on the vertical of the underground Laboratori Nazionali del Gran Sasso (LNGS), which provided logistical support. This accommodation is a reasonable compromise between ideal places not easily accessible (like Antarctica) or isolated places with no facilities available (like White Mountain [California] or Alpe Gera [Italian Alps]) we used in the past.

Various tests were made at Campo Imperatore between 1991 and 1995. They showed that in spite of the mountain circle, interferences from horizon directions were occasionally present and forced us to observe only at the zenith. The final installation of TRIS radiometers was made between summer 1997 and summer 1998. After repeated observations dedicated to find clean frequency channels, differential measurements (drift scans) began. They continued in 1999 when tests of the cryogenic front ends were completed. Absolute measurements of the sky temperature were made in 2000 June and October. Drift scans were then resumed and continued until 2001 May when antennas were removed from Campo Imperatore.

4.1. Modes of Operation

Three modes of operation have been used with TRIS:

1. *Interference search mode.*—The PC drives the local oscillator and tunes cyclically the receiver through the 256 frequencies distributed around the receiver nominal frequency ν_0 (10 minutes channel⁻¹). Simple statistics (mean and standard deviation) have been used to recognize channels disturbed by interferences and to choose quiet channels where observations were possible. Searches lasting at least 24 hr were repeated at various epochs. At 0.6 and 0.82 GHz we found frequencies free from interferences. The best were 0.6005 and 0.8178 GHz. At 2.5 GHz no frequency completely free from interferences was found. The best one was 2.4278 GHz. These frequencies are those used for the final observations in both the following modes.

2. *Absolute measurement mode.*—The antenna is aimed at the zenith. The horn throat is attached to the collar of the cryogenic front end. A couple of hours after filling (or partial refilling) with LHe, the system is in thermal equilibrium and observations are possible. Moving the switch manually, the receiver input is cyclically connected to the cold source (receiver output S_{cold}), the antenna (receiver output S_{sky}), and the warm source (receiver output S_{warm}). Each step of the cycle lasts 10 minutes, during which

15 records minute⁻¹ are stored on the PC hard disk. Each record contains S_x , UT time, Julian day, temperature of loads and lossy components between switch and antenna mouth, and housekeeping data. The cycle of three steps is repeated a few times, then the switch is set on the antenna position and observation goes on for about 1 hr recording S_{sky} . At regular time intervals the solid-state noise source is set on and data necessary to check gain stability and power reflection coefficients r^2 of the source at the receiver input are recorded. Absolute measurements are made only at nighttime, when the observing conditions are good and the dewar is full of LHe well above the top of the waveguide coaxial transition. At 0.6 GHz observations with the cryogenic waveguide went on regularly. At 0.82 GHz we began observation in June using the cryogenic front end, but the dewar failed because of a leakage in the vacuum tank. We fixed it, but in October, when after the 0.6 GHz run we moved at 0.82 GHz, the dewar failed again and we had no possibility to fix it again before leaving Campo Imperatore. So at 0.82 GHz we have only absolute measurements made as preliminary tests in June, using the cryogenic switch cooled with liquid helium and the completely warm antenna. This system worked very efficiently, but because all the horn components, including the waveguide-coaxial transition, were at ambient temperature, final results at 0.82 GHz are less accurate than at 0.6 GHz. The absolute measurements at 2.5 GHz with the cryogenic waveguide went on regularly but were plagued by interferences.

3. *Drift-scan mode.*—Records with S_{sky} and the associated information are stored continuously every 4 s while the sky transits through the antenna beam aimed at the zenith. In this mode we look at the variations of S_{sky} with right ascension and do not care about the signal zero level, provided that it is stable. The antenna can be attached to the dewar (no matter if cold or warm) with the switch on position 2 or attached directly to the receiver via an ambient temperature coaxial-waveguide transition. Gain stability and antenna power reflection coefficient are measured automatically two times per hour. In this mode the radiometers can work unattended for weeks. Because data collected at daytime and more noticeably around noon are usually contaminated by the Sun emission, to cover the entire $0^{\text{h}}\text{--}24^{\text{h}}$ right ascension interval, drift scans are repeated months apart. Drift-scan data were collected during the entire lifetime of TRIS. The more systematic observations were made from 1998 on. At 0.6 and 0.82 GHz they are sufficient to cover the entire 24^{h} circle of right ascension at $\delta = +42^\circ$. At 2.5 GHz the great majority of the observations were disturbed by interferences and no complete drift scans were obtained.

4.2. Data Reduction

First of all, the raw data collected in absolute or drift-scan mode are *edited*. We reject all the records containing data obtained (1) at daytime (between half an hour before sunrise and half an hour after sunset); (2) less than 6 hr after the receiver was turned on; or when (3) interferences were evident on the records, (4) the log book shows that the weather conditions were bad (rain, snow), (5) the antenna reflection coefficients r^2 monitored by the receiver internal reflectometer worsened (e.g., because of water vapor condensation on the antenna components at sunrise or sunset), or (6) the system gain or the noise level changes or fluctuates by more than 5%.

The remaining data are then divided into blocks, continuous time series of homogeneous records, lasting at least 10 minutes. A block starts when the switch is set in a position (or when drift-scan mode starts) and stops when the switch is moved to a new position or whenever a major interruption of the time series occurs.

We call them absolute sky, cold, warm, and drift-scan or differential blocks (or records, or data), depending on the observing mode and/or the switch position. Typical block lengths are 5–20 minutes for absolute data. The blocks of differential data can last hours.

Then we remove all the data collected in the first minute of a block time series (to account for the response time of the system) and continuous time series of differential data lasting less than 3 hr and separated from the following homogeneous block of data used for analysis by more than 1 hr.

Finally, for each record we calculate and add to it (α , δ) of the antenna beam axis calculated from the recorded values of time and Julian day, the effective noise temperatures radiated by the receiver T_{RX}^{eff} ,³ and the effective noise temperatures of cold load, warm load, and circulator third port, respectively, $T_{\text{cold}}^{\text{eff}}$, $T_{\text{warm}}^{\text{eff}}$, and T_N^{eff} using equation (7).

The resulting blocks are the data ready to be analyzed. They are treated in different ways, depending on their type.

4.3. Absolute Values of Sky Temperature

From pairs of time adjacent blocks of *cold* and *warm data* the gain G is obtained using equation (6) and the average values of S_{cold} , $T_{\text{cold}}^{\text{eff}}$, S_{warm} , and $T_{\text{warm}}^{\text{eff}}$ on the block. Typical values are shown in Table 5.

Then from each value of S_{sky} in a *sky* block and G from the nearest pair of *cold* and *warm data* we get the instantaneous value of the signal temperature that arrives at the switch:

$$T_{a,sw} = T_{\text{cold}}^{\text{eff}} + (S_{\text{sky}} - S_{\text{cold}})G. \quad (10)$$

The system linearity, i.e., the stability of G and its independence on the signal level, has been checked during all the calibration campaigns, by looking at the amplitude of the calibration mark (CM) when injected over very different levels of signals: cold load (He), sky, and warm load. It is worthwhile to underline that the CM provides an equivalent temperature in the same range of the maximum variation of antenna temperature measured by our experiment (about 20, 14, and 1 K at 0.6, 0.82, and 2.5 GHz, respectively). CM amplitude was constant within statistical fluctuations, setting a 0.4% upper limit to the deviation from system linearity.

The antenna temperature at the horn mouth is then

$$T_a(\alpha, \delta) = \frac{1}{1 - r^2} \left\{ \left[\frac{T_{a,sw} - \int_0^{\tau_{tl}} T_{tl}(x) e^{-\tau_{tl}(x)} d\tau}{e^{-\tau_{tl}} e^{-\tau_h}} - \frac{\int_0^{\tau_h} T_h(x) e^{-\tau_h(x)} d\tau}{e^{-\tau_h}} \right] - r^2 T_{RX}^{\text{eff}} \right\}. \quad (11)$$

Here T_{tl} , τ_{tl} , T_h , and τ_h are the temperatures and the optical thicknesses of the lossy components along the transmission line (tl) and the horn sections (h) between the switch and the antenna aperture.

4.3.1. Sky Temperature

The sky brightness temperature is then

$$T_{\text{sky}}(\alpha, \delta, \nu) = \frac{[T_a(\alpha, \delta, \nu) - T_{RX} r^2] / (1 - r^2) - T_{\text{atm}}^0 (1 - e^{-\tau_{\text{atm}}}) - T_{\text{env}}}{e^{-\tau_{\text{atm}}}}, \quad (12)$$

³ When loads are well matched in eq. (7), we can set $r^2 \simeq 0$, get the effective temperature of the circulator third port T_N^{eff} , and set it equal to T_{RX}^{eff} . Then we repeat the calculation of the effective noise temperature of the circulator third port as seen at the switch and use this value as final T_{RX}^{eff} .

TABLE 6
ATMOSPHERIC AND ENVIRONMENT CONTRIBUTIONS

Parameter	$\nu_0 = 0.60$ GHz	$\nu_0 = 0.82$ GHz	$\nu_0 = 2.5$ GHz
T_{atm} (K)	1.088 ± 0.023	1.221 ± 0.016	1.570 ± 0.025
$e^{-\tau_{\text{atm}}}$	0.995 ± 0.001	0.995 ± 0.001	0.993 ± 0.001
T_{ground} (K)	$0.07^{+0.06}_{-0.03}$	$0.07^{+0.06}_{-0.03}$	$0.07^{+0.06}_{-0.03}$
T_{interf} (K)	<0.01	<0.01	9.82 ± 0.26

where τ_{atm} and T_{atm}^0 are the optical thickness and the average physical temperature of the atmosphere above the antenna, respectively; T_{env} is the noise temperature of the environment that reaches the antenna, usually through side and back lobes; $T_{\text{RX}}^{\text{eff}}$ is the temperature of the noise radiated by the radiometer; and r^2 is the power reflection coefficient of the antenna.

At nighttime, when the Sun contamination is absent, $T_{\text{env}} = T_{\text{ground}} + T_{\text{interf}}$, where T_{ground} , the effect of the ground thermal emission, is the convolution of $P_n(\theta, \phi)$, the normalized, three-dimensional, beam profile (see Fig. 2), and a blackbody at ambient temperature T_0 , which fills the antenna beam up to $h(\phi)$, the Campo Imperatore horizon profile (see Fig. 3):

$$T_{\text{ground}} = T_0 \int_0^{2\pi} d\phi \int_0^{h(\phi)} P_n(\theta, \phi) \sin \theta d\theta. \quad (13)$$

T_{interf} is the noise produced by radio interferences. At 0.6 and 0.82 GHz channels free from interferences were found (0.6005 and 0.8178 GHz). Here the interferences, if present, were completely buried in the system noise. At 2.5 GHz also in the best channel at 2.4278 GHz, even when no sudden changes of level were appreciable, the signal was unstable and the noise anomalously high, probably because of a blend of undesired signal from artificial sources at the horizon or below it. This contribution has been measured surrounding the antenna with ground shields that went well above the horizon visible from the antenna mouth and reflected all the side and back lobes on the sky.

For the atmospheric contributions we use values of absorption calculated for various sites, including Campo Imperatore, by Ajello et al. (1995) from a collection of vertical profiles of the Earth atmosphere collected for 1 yr with sounding balloons launched daily at meteo stations. Results are shown in Table 6.

The above values of T_{sky} , T_a , and $T_{a,sw}$ are oversampled because the TRIS sampling time (4 s) is shorter than the system time constant (10 s). To make them statistically independent in each sky block, data are binned in groups of at least 50 s and averaged. The average values and standard deviations of T_{sky} in a bin are considered representative of the absolute brightness temperature of the sky at ($\langle\alpha\rangle$, $\langle\delta\rangle$) only if they come from a block close (few tens of minutes) to the pair of cold and warm data used to get G and $T_{\text{cold}}^{\text{eff}}$. This is because G and $T_{\text{cold}}^{\text{eff}}$ are helium level dependent and the level is practically constant within this period of time.

4.4. Drift Scans of the Sky Temperature

The edited time series of drift-scan data are from observations made in separate years at different times of the year, in different conditions.

During the drift-scan mode observations, every component of the radiometers was at ambient temperature, with the receivers always operating in a temperature-controlled box. In this configuration, the data were taken continuously for months. We decided to reject daytime data. Moreover, bad weather conditions

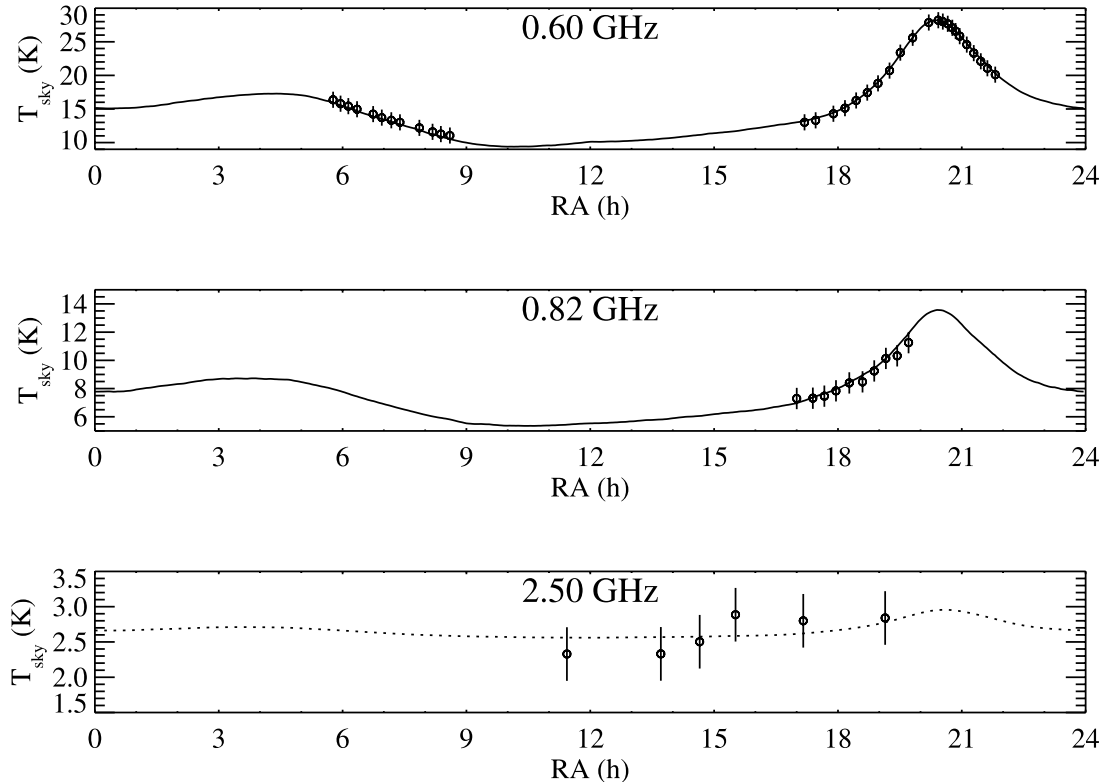


FIG. 5.—Absolute values and differential profiles of T_{sky} measured by TRIS at $\delta = +42^\circ$, $0^{\text{h}} \leq \alpha \leq 24^{\text{h}}$. Uncertainties (3σ statistic + systematic) associated with the absolute values are indicated: to make them visible at 0.60 GHz, the error bars have been enlarged by a factor of 10. The zero level of the differential profiles has been adjusted to fit the distribution vs. α of the absolute values. At 2.50 GHz the plotted sky profile (*dashed line*) does not come from TRIS data, but it has been obtained rescaling the sky profile extracted from the Stockert (Reich & Reich 1986) survey at 1.4 GHz. See Paper III for details.

and interferences did not allow us to exploit all the nighttime data collected; therefore, it took more than 1 yr to cover all the $\delta = +42^\circ$ sky circle since the last TRIS configuration (antennas in vertical position, receivers in total power configuration) was established. We combined data taken at different times by virtue of the internal and stable noise source (CM), whose signal was periodically (two times every 48 minutes) injected toward the antenna port of the circulator in order to check the SWR (reflector mode) and, after that, toward the receiver port as a CM.⁴ In this way, we could associate a value of the CM to every set of observations. The different sets were then normalized to the reference CM measured during absolute calibrations. We have been able to find time sequences of good data (good weather conditions, no radio interferences) lasting more than 48 hr. This allowed us to compare nighttime data separated up to 2 sidereal days and correct for linear drifts of the signal (if present). The nighttime data, corrected for drift and renormalized by means of the CM, have been seamed at common right ascension. Integration of all the nighttime profiles acquired during the life of the experiment gives the final profile. Its scale, in ADU and arbitrary zero level, was then converted to temperature scale and zero adjusted fitting the profile to the absolute values of sky temperature measured during calibration sessions. The reconstruction of the full sky profiles at 0.6 and 0.82 GHz deserves some other comments. The CM signals have a very small dispersion, witnessing the stability of the system all along the observational campaign. In fact, the sample collected during several months at 0.6 GHz had a mean value around 24,000 ADU, while the mean standard deviation set

around 20 ADU. The corresponding quantities at 0.82 GHz were, respectively, 19,500 and 30 ADU.

The error budget on the two definitive profiles at 0.6 and 0.82 GHz is then dominated by the uncertainties due to the correction for the linear drifts and offsets and by the uncertainty in the determination of the temperature scale. In particular, along the Galactic halo region ($8^{\text{h}} \lesssim \alpha \lesssim 16^{\text{h}}$), which has been observed redundantly, the definitive uncertainty on temperature variations is in the range 5–10 mK at both 0.6 and 0.82 GHz, depending on the sky position (this uncertainty rises to 30–40 mK near the Galactic plane, where we have collected a smaller number of drift scans).

By this procedure we recover the full dynamic of the celestial signal up to the antenna mouth and above the Earth atmosphere. Results are shown in Figure 5. This procedure worked successfully at 0.6 and 0.82 GHz. At 2.5 GHz the construction of drift-scan profile was hampered by the interference level that frequently covered the sky signal. The few observing hours when interferences were small are so sparse that we could not build a clean drift-scan profile.

5. DISCUSSION

The absolute values of $T_{\text{sky}}(\alpha, \delta)$ measured by TRIS at 0.6005, 0.8178, and 2.4278 GHz, at selected points of constant declination $+42^\circ$, are listed in Tables 7, 8, and 9, respectively. The same data are plotted in Figure 5 together with the drift scans (0.6 and 0.82 GHz are reported in Tables 10 and 11). Having no reliable drift scan at 2.5 GHz, we built a profile only of the Galactic component starting from the Stockert (Reich & Reich 1986) survey at 1.420 GHz. This map has been convoluted to the beam of the TRIS antennas in order to get the synthetic drift scan at $\delta = +42^\circ$. Then

⁴ The CM is the value above the noise floor of the signal injected by the noise generator, expressed in ADU. The gain is properly the conversion factor K ADU^{-1} .

TABLE 7
ABSOLUTE VALUES OF T_{sky} AT $\nu = 0.60$ GHz, $\delta = +42^\circ$

α	T_{sky}^a (K)	α	T_{sky}^a (K)	α	T_{sky}^a (K)
05 46 00.....	16.372	17 11 18.....	13.016	20 32 35.....	28.007
05 57 02.....	15.788	17 27 31.....	13.315	20 39 18.....	27.678
06 08 26.....	15.423	17 53 37.....	14.292	20 45 59.....	27.084
06 20 46.....	14.962	18 10 12.....	15.123	20 50 46.....	26.592
06 44 22.....	14.241	18 26 23.....	16.267	20 57 11.....	25.839
06 57 14.....	13.717	18 42 33.....	17.437	21 07 13.....	24.582
07 10 34.....	13.319	18 58 24.....	18.813	21 17 17.....	23.312
07 23 18.....	13.010	19 14 56.....	20.715	21 27 18.....	22.100
07 51 39.....	12.193	19 30 39.....	23.386	21 37 20.....	21.061
08 10 34.....	11.602	19 48 22.....	25.593	21 48 40.....	20.107
08 22 56.....	11.264	20 12 02.....	27.869		
08 36 02.....	11.050	20 25 52.....	28.211		

NOTE.—Units of right ascension are hours, minutes, and seconds.
^a For error bars see Table 12.

we compared this scan with the pure Galactic signal we evaluated at 0.6 and 0.82 GHz (see Papers II and III). Using these measurements, we evaluated the Galactic emission first at 1.420 GHz and then extrapolated it at 2.5 GHz, using the local spectral index evaluated between 0.6 and 0.82 GHz. We used the local spectral index because it is a well-defined quantity throughout all the sky provided that absolute Galactic emission measurements are available, which is our case. We used the map at 1.42 GHz because it is the closest one, public domain, at the frequency 2.5 GHz. In Figure 5 at 2.5 GHz, for uniformity with the measured sky profiles plotted at 0.6 and 0.82 GHz, we added over the TRIS absolute sky temperatures a profile (*dashed line*) obtained summing to the Galactic component calculated as described above, the unresolved extragalactic radio source contribution (Gervasi et al. 2008a) and cosmic microwave background (Paper II).

The systematic uncertainties are computed propagating through equations (11) and (12) the uncertainties on the measured values of attenuation and temperature of the lossy components between the switch and the antenna mouth. The losses are very small. In some cases they are so small that measurements give only upper limits (see Table 4) and the range of fluctuation of the true losses is unknown but reasonably smaller and well inside the upper limit, set by the accuracy of the instrumentation used to carry on the measurements. The final uncertainties on the sky temperature obtained propagating these errors are therefore considered as systematic. At 0.6 GHz the great majority of the components are cold (~ 4 K) and the final systematic uncertainty is small (66 mK). At 2.5 GHz the systematic uncertainty is worse because of the quality of the electromagnetic matching of the SPTT switch and the presence of an additional section of warm waveguide between the dewar flange and the antenna throat. This correction contributes to the system-

TABLE 8
ABSOLUTE VALUES OF T_{sky} AT $\nu = 0.82$ GHz, $\delta = +42^\circ$

α	T_{sky}^a (K)	α	T_{sky}^a (K)	α	T_{sky}^a (K)
17 00 04.....	7.297	18 16 29.....	8.401	19 26 04.....	10.322
17 23 29.....	7.319	18 35 40.....	8.476	19 42 39.....	11.256
17 40 15.....	7.463	18 52 43.....	9.249		
17 57 06.....	7.840	19 09 38.....	10.137		

NOTE.—Units of right ascension are hours, minutes, and seconds.
^a For error bars see Table 12.

TABLE 9
ABSOLUTE VALUES OF T_{sky} AT $\nu = 2.5$ GHz, $\delta = +42^\circ$

α	T_{sky}^a (K)	α	T_{sky}^a (K)	α	T_{sky}^a (K)
11 26 04.....	2.329	14 39 01.....	2.503	17 09 34.....	2.800
13 42 32.....	2.331	15 31 06.....	2.886	19 08 35.....	2.840

NOTE.—Units of right ascension are hours, minutes, and seconds.
^a For error bars see Table 12.

atics for 284 mK. At 0.82 GHz the systematic uncertainty is very large, 660 mK, essentially because all the components above the switch were warm and at high temperature (see eq. [9]). Such a large value, however, does not take into account constraints set by unphysical situations (e.g., negative values of the temperature of the diffuse radiation components and values of the Galactic spectral index not supported by models of Galactic emission). When astrophysical assumptions are made on these values (for a complete discussion see Paper III), the systematic uncertainty at 0.82 GHz is reduced to $^{+430}_{-300}$ mK.

The above results hold if the sky radiation is unpolarized. We know, however, that the Galactic component of T_{sky} is partially polarized and that polarization is linear. Since antennas are polarized, our measured values of the sky temperature are better written as

$$T_{\text{sky}}(\alpha, \delta, \nu) = T_{\text{CMB}}(\nu) + T_{\text{UERS}}(\nu) + T_{\text{Gal}}^{\text{unpol}}(\alpha, \delta, \nu) + T_{\text{Gal}}^{\text{pol}}(\alpha, \delta, \nu) \cos^2[\theta(\alpha, \delta, \nu) - \theta_0], \quad (14)$$

where $T_{\text{Gal}}^{\text{unpol}}$ and $T_{\text{Gal}}^{\text{pol}}$ are, respectively, the unpolarized and polarized components of the Galactic signal and $(\theta - \theta_0)$ is the angle between the polarization vector of the radiation and the polarization vector of the antenna. The true sky temperature is therefore

$$T_{\text{sky}}^{\text{true}}(\alpha, \delta, \nu) = T_{\text{sky}}^{\text{unpol}}(\alpha, \delta, \nu) + T_{\text{sky}}^{\text{pol}}(\alpha, \delta, \nu) = T_{\text{sky}}(\alpha, \delta, \nu) + \Delta T^{\text{pol}}(\alpha, \delta, \nu), \quad (15)$$

TABLE 10
SAMPLED VALUES OF T_{sky} PROFILE AT $\nu = 0.60$ GHz, $\delta = +42^\circ$

α	T_{sky}^a (K)	α	T_{sky}^a (K)	α	T_{sky}^a (K)
00 00 00.....	15.145	08 00 00.....	11.552	16 00 00.....	12.117
00 30 00.....	15.099	08 30 00.....	10.683	16 30 00.....	12.585
01 00 00.....	15.204	09 00 00.....	9.996	17 00 00.....	13.023
01 30 00.....	15.494	09 30 00.....	9.576	17 30 00.....	13.703
02 00 00.....	15.986	10 00 00.....	9.390	18 00 00.....	14.747
02 30 00.....	16.343	10 30 00.....	9.412	18 30 00.....	16.543
03 00 00.....	16.745	11 00 00.....	9.572	19 00 00.....	19.201
03 30 00.....	17.046	11 30 00.....	9.801	19 30 00.....	23.044
04 00 00.....	17.242	12 00 00.....	10.124	20 00 00.....	27.015
04 30 00.....	17.275	12 30 00.....	10.168	20 30 00.....	28.048
05 00 00.....	17.050	13 00 00.....	10.273	21 00 00.....	25.628
05 30 00.....	16.395	13 30 00.....	10.442	21 30 00.....	22.210
06 00 00.....	15.443	14 00 00.....	10.719	22 00 00.....	19.323
06 30 00.....	14.368	14 30 00.....	11.058	22 30 00.....	17.342
07 00 00.....	13.438	15 00 00.....	11.397	23 00 00.....	16.204
07 30 00.....	12.506	15 30 00.....	11.682	23 30 00.....	15.474

NOTE.—Units of right ascension are hours, minutes, and seconds.
^a For error bars see Table 12.

TABLE 11
SAMPLED VALUES OF T_{sky} PROFILE AT $\nu = 0.82$ GHz, $\delta = +42^\circ$

α	T_{sky}^a (K)	α	T_{sky}^a (K)	α	T_{sky}^a (K)
00 00 00.....	7.781	08 00 00.....	6.145	16 00 00.....	6.481
00 30 00.....	7.781	08 30 00.....	5.869	16 30 00.....	6.707
01 00 00.....	7.935	09 00 00.....	5.537	17 00 00.....	6.969
01 30 00.....	8.143	09 30 00.....	5.471	17 30 00.....	7.486
02 00 00.....	8.322	10 00 00.....	5.371	18 00 00.....	8.026
02 30 00.....	8.529	10 30 00.....	5.357	18 30 00.....	8.783
03 00 00.....	8.678	11 00 00.....	5.387	19 00 00.....	9.724
03 30 00.....	8.718	11 30 00.....	5.456	19 30 00.....	11.198
04 00 00.....	8.702	12 00 00.....	5.536	20 00 00.....	12.905
04 30 00.....	8.648	12 30 00.....	5.589	20 30 00.....	13.555
05 00 00.....	8.465	13 00 00.....	5.679	21 00 00.....	12.547
05 30 00.....	8.141	13 30 00.....	5.778	21 30 00.....	11.141
06 00 00.....	7.772	14 00 00.....	5.897	22 00 00.....	9.839
06 30 00.....	7.307	14 30 00.....	6.026	22 30 00.....	8.823
07 00 00.....	6.902	15 00 00.....	6.185	23 00 00.....	8.235
07 30 00.....	6.512	15 30 00.....	6.331	23 30 00.....	7.924

NOTE.—Units of right ascension are hours, minutes, and seconds.

^a For error bars see Table 12.

where

$$\Delta T^{\text{pol}}(\alpha, \delta, \nu) = T_{\text{Gal}}^{\text{pol}}(\alpha, \delta, \nu) \sin^2[\theta(\alpha, \delta, \nu) - \theta_0] \quad (16)$$

is the signal lost. Were circular polarization present, an additional term should be added to equation (15).

The information today available on the polarization degree and direction of the diffuse radiation is limited. We do not expect circular polarization. Linear polarization, on the contrary, must be expected, but the information available is poor. Below 1 GHz there are only data obtained 30 years ago by Brouw & Spoelstra (1976). The assessment of the overall sky temperature has been obtained correcting our absolute measurements for the fraction of the linearly polarized signal. In order to do this, we used the Brouw and Spoelstra maps of the Stokes parameters Q and U in the resampled version prepared by E. Carretti in the framework of the *SPOrt* program (Cortiglioni et al. 2004). Carretti maps having 7° resolution were further convolved with the beam of our experiment. Then, considering the relative orientation of the polarization plane (E-plane) of our antennas and the polarization of the celestial signal, we projected the polarized vector into copolar (collected by our antennas) and cross-polar components (rejected by our antennas). We conclude that, at TRIS angular resolution, the maximum contribution of the polarized signal to the overall one, around 2% at 0.6 GHz and 3% at 0.82 GHz, comes mostly from regions far from the Galactic disk. This result is in agreement with Platania et al. (1998), who give a maximum contribution of $\sim 5\%$ at 0.408 GHz with an 18° beam in a sky

TABLE 13
ACCURACY OF MEASUREMENTS IN LITERATURE OF T_{CMB} AND T_{sky}
AT FREQUENCIES CLOSE TO 0.6, 0.82 AND 2.5 GHz

ν (GHz)	λ (cm)	σ_{sky} (K)	T_{CMB} (K)	σ_{CMB} (K)	References
0.610.....	49.1	0.7	3.7	1.2	1
0.6.....	50.0	0.9	3.0	1.2	2
0.635.....	47.2	~ 0.5	3.0	0.5	3
0.82.....	36.6	1.5	2.7	1.6	4
2.....	15	≤ 0.3	2.5	0.3	5
2.....	15	0.10	2.55	0.14	6
2.3.....	13.1	0.2–0.4	2.66	0.7	7
2.5.....	12	0.15	2.5	0.21	4

REFERENCES.—(1) Howell & Shakeshaft 1967; (2) Sironi et al. 1990; (3) Stankevich et al. 1970; (4) Sironi et al. 1991; (5) Pelyushenko & Stankevich 1969; (6) Bersanelli et al. 1994; (7) Otoshi & Stelzried 1975.

region very close to the one scanned by TRIS. A detailed discussion can be found in Paper III. Between 1 and 3 GHz more recent and accurate data are available (see, e.g., Duncan et al. 1999; Wolleben et al. 2006 and references therein), but with few exceptions they do not fill all the areas covered by TRIS scans. Full sky models of the Galactic synchrotron intensity and linear polarization prepared for feasibility studies of forthcoming space experiments (e.g., Giardino et al. 2002; Bernardi et al. 2003) are available. However, we preferred to evaluate the polarized component starting from real data acquired at frequencies close to the TRIS ones. Considering that at 2.5 GHz with the TRIS angular resolution $T_{\text{Gal}}/T_{\text{sky}} \simeq T_{\text{Gal}}/T_{\text{CMB}} \leq 0.1$ and $T_{\text{Gal}}^{\text{pol}} \leq T_{\text{Gal}}$, we can assume also at 2.5 GHz that $\Delta T^{\text{pol}}/T_{\text{sky}}^{\text{true}} < 0.02$.

In conclusion, neglecting the polarization effects is equivalent to introducing an additional systematic uncertainty on the true values of the sky temperature of less than 3% (see Table 12).

Table 13 gives a list of measurements of T_{sky} present in literature at frequencies comparable to the frequencies used by TRIS, the value of the derived T_{CMB} , and the associated uncertainties for T_{sky} and T_{CMB} . All the values of T_{sky} have been obtained as intermediate steps of experiments aimed at getting the CMB temperature, so papers usually focus the reader's attention on the accuracy σ_{CMB} of T_{CMB} . The accuracy σ_{sky} of T_{sky} should be better ($\sigma_{\text{sky}} < \sigma_{\text{CMB}}$), but extracting it from papers is not always possible. When no detailed information is available in literature, we assume $\sigma_{\text{sky}} \leq \sigma_{\text{CMB}}$. It appears that at 0.6 and 0.82 GHz the TRIS absolute values of the sky temperature are the best today available. At 2.5 GHz TRIS results are less accurate than data obtained in the past by us with the White Mountain and the South Pole collaborations. Nevertheless, we report also the TRIS results at 2.5 GHz because they came exactly from the same direction and have been obtained with the same angular resolution of our observation at lower frequencies.

TABLE 12
ACCURACY OF THE ABSOLUTE VALUES OF T_{sky} MEASURED BY TRIS AT $\delta = +42^\circ$

Parameter	$\nu = 0.60$ GHz	$\nu = 0.82$ GHz	$\nu = 2.5$ GHz
Statistical uncertainty:			
Standard deviation σ (mK).....	104	160	25
Mean standard deviation σ_m (mK).....	18	32	10
Systematic uncertainty:			
Zero level (mK).....	66	$^{+430}_-300$ ^a	284
Polarization effect (%).....	<2	<3	<2

^a See § 5.

TABLE 14
TRIS RESULTS SUMMARY

Parameter	$\alpha^1 = 10^{\text{h}}00^{\text{m}}$	$\alpha^2 = 20^{\text{h}}24^{\text{m}}$
$\nu = 0.6 \text{ GHz}$		
T_{sky} (K).....	9.390 ± 0.066 (syst) ± 0.018 (stat)	28.190 ± 0.066 (syst) ± 0.018 (stat)
T_{Gal} (K).....	5.72 ± 0.07	24.44 ± 0.07
T_{UERS} (K).....	0.934 ± 0.024	0.934 ± 0.024
T_{CMB} (K).....	2.823 ± 0.066 (syst) ± 0.129 (MC) ^a	2.823 ± 0.066 (syst) ± 0.129 (MC) ^a
$T_{\text{CMB}}^{\text{th}}$ (K).....	2.837 ± 0.066 (syst) ± 0.129 (MC) ^a	2.837 ± 0.066 (syst) ± 0.129 (MC) ^a
$\nu = 0.82 \text{ GHz}$		
T_{sky} (K).....	$5.37^{+0.46}_{-0.30}$ (syst) ± 0.03 (stat)	$13.57^{+0.46}_{-0.30}$ (syst) ± 0.03 (stat)
T_{Gal} (K).....	2.21 ± 0.03	10.38 ± 0.03
T_{UERS} (K).....	0.408 ± 0.010	0.408 ± 0.010
T_{CMB} (K).....	$2.783^{+0.430}_{-0.300}$ (syst) ± 0.051 (MC) ^a	$2.783^{+0.430}_{-0.300}$ (syst) ± 0.051 (MC) ^a
$T_{\text{CMB}}^{\text{th}}$ (K).....	$2.803^{+0.430}_{-0.300}$ (syst) ± 0.051 (MC) ^a	$2.803^{+0.430}_{-0.300}$ (syst) ± 0.051 (MC) ^a
$\nu = 2.5 \text{ GHz}$		
T_{sky} (K).....	2.57 ± 0.28 (syst) ± 0.10 (stat)	2.99 ± 0.28 (syst) ± 0.10 (stat)
$T_{\text{Gal}}^{\text{b}}$ (K).....	0.091 ± 0.093 (syst) ± 0.005 (stat)	0.471 ± 0.093 (syst) ± 0.027 (stat)
T_{UERS} (K).....	0.022 ± 0.001	0.022 ± 0.001
T_{CMB} (K).....	2.458 ± 0.284 (syst) ± 0.139 (stat)	2.458 ± 0.284 (syst) ± 0.139 (stat)
$T_{\text{CMB}}^{\text{th}}$ (K).....	2.516 ± 0.284 (syst) ± 0.139 (stat)	2.516 ± 0.284 (syst) ± 0.139 (stat)

^a This uncertainty was evaluated by means of Monte Carlo simulations, as described in Paper II.

^b Due to the incompleteness of the TRIS drift scan at 2.5 GHz, here T_{Gal} is extrapolated by the Reich & Reich (1986) map at 1.42 GHz convolved with the TRIS beam and using the local spectral index calculated from our data at 0.6 and 0.82 GHz. The quoted systematic uncertainty for T_{Gal} is relative to the determination of the Galactic signal at 1.42 GHz, starting from the absolute measurements at 0.6 and 0.82 GHz.

TRIS data can be used to (1) disentangle the components of the diffuse radiation, (2) extract the cosmological and astrophysical information carried by these components, and (3) improve zero level and scale of temperature of the full sky maps of the diffuse radiation at decimetric wavelength in literature (see Tables 1 and 2).

These types of analysis are intricate and require different approaches, depending on the final aim: astrophysical or cosmological conclusion. They are done in Papers II and III and Gervasi et al. (2008a), which accompany the present Paper I. Here (Table 14) we present a summary of the results discussed in the cited papers. We have reduced the error bars on T_{CMB} of a factor of 9 at $\nu = 0.6 \text{ GHz}$ and of a factor of 7 at $\nu = 0.82 \text{ GHz}$. These results have been possible because of the improvements in the absolute calibration system and in the foreground separation technique. At 2.5 GHz TRIS did not improve the previous measurements but is in agreement with them.

The TRIS activity has been supported by MIUR (Italian Ministry of University and Research), CNR (Italian National Council of Research), and the Universities of Milano and of Milano-Bicocca. The logistic support at Campo Imperatore was provided by INFN, the Italian Institute of Nuclear Physics, and its Laboratorio Nazionale del Gran Sasso. We are indebted to E. Carretti, who provided us a low-resolution polarized map based on the Brouw and Spoelstra one. We are also grateful to R. Nesti for some crucial simulations of the horn attenuations. We acknowledge the contributions and comments by many people, among them G. Bonelli, A. Grillo, C. Cattadori, G. De Amici, E. Pagana, G. Navarra, and members of the LNGS technical staff A. Fulgenzi, G. Adinolfi, L. Masci, and G. Giuliani. Frequently students who were preparing their thesis for the degree in Physics took part in TRIS activities. We acknowledge the use of the HEALPix package (Gorski et al. 2005) to evaluate the polarized Galactic signal at 0.610 and 0.82 GHz.

REFERENCES

- Ajello, C., Bonelli, G., & Sironi, G. 1995, *ApJS*, 96, 643
 Bensadoun, M., Bersanelli, M., de Amici, G., Kogut, A., Levin, S. M., Limon, M., Smoot, G. F., & Witebsky, C. 1993, *ApJ*, 409, 1
 Bensadoun, M., Witebsky, C., Smoot, G., de Amici, G., Kogut, A., & Levin, S. 1992, *Rev. Sci. Instrum.*, 63, 4377
 Berkhuijsen, E. M. 1972, *A&AS*, 5, 263
 Bernardi, G., Carretti, E., Cortiglioni, S., Sault, R. J., Kesteven, M. J., & Poppi, S. 2003, *ApJ*, 594, L5
 Bersanelli, M., Bensadoun, M., de Amici, G., Levin, S., Limon, M., Smoot, G. F., & Vinje, W. 1994, *ApJ*, 424, 517
 Bersanelli, M., et al. 1993, *Antarctic J.* XXVIII, 306
 Brouw, W. N., & Spoelstra, T. A. T. 1976, *A&AS*, 26, 129
 Burigana, C., & Danese, L., & de Zotti, G. 1991, *A&A*, 246, 49
 Committee on Extensions to the Standard Atmosphere. 1976, *US Standard Atmosphere 1976* (Washington: GPO)
 Cortiglioni, S., et al. 2004, *NewA*, 9, 297
 Duncan, A. R., Reich, P., Reich, W., & Fuerst, E. 1999, *A&A*, 350, 447
 Fixsen, D. J., & Mather, J. C. 2002, *ApJ*, 581, 817
 Gervasi, M., Tartari, A., Zannoni, M., Boella, G., & Sironi, G. 2008a, *ApJ*, 682, 223
 Gervasi, M., Zannoni, M., Tartari, A., Boella, G., & Sironi, G. 2008b, *ApJ*, 688, 24 (Paper II)
 Giardino, G., Banday, A. J., Górski, K. M., Bennet, K., Jonas, J. L., & Tauber, J. 2002, *A&A*, 387, 82
 Gorski, K. M., Hivon, E., Banday, A. J., Wandelt, B. D., Hansen, F. K., Reinecke, M., & Bartelmann, M. 2005, *ApJ*, 622, 759
 Haslam, C. G. T., Salter, C. J., Stoffel, H., & Wilson, W. E. 1982, *A&AS*, 47, 1
 Howell, T. F., & Shakeshaft, J. R. 1967, *Nature*, 216, 753
 Jonas, J., Baart, E. E., & Nicolson, G. D. 1998, *MNRAS*, 297, 977
 Kogut, A., Fixsen, D. J., Levin, S., Limon, M., Lubin, P. M., Mirel, P., Seiffert, M., & Wollack, E. 2004, *ApJS*, 154, 493
 Kogut, A., et al. 2006, *NewA Rev.*, 50, 925
 Landecker, T. L., & Wielebinsky, R. 1970, *Australian J. Phys. Astrophys. Suppl.*, 16, 1

- Mather, J. C., et al. 1994, ApJ, 420, 439
- Milogradov-Turin, J., & Smith, F. G. 1973, MNRAS, 161, 269
- Otoshi, T. Y., & Stelzried, C. T. 1975, IEEE Trans. Instrum. Meas., 24, 174
- Pelyushenko, S. A., & Stankevich, K. S. 1969, Soviet Astron., 13, 223
- Platania, P., Bensadoun, M., Bersanelli, M., De Amici, G., Kogut, A., Levin, S., Maino, D., & Smoot, G. F. 1998, ApJ, 505, 473
- Platania, P., Burigana, C., Maino, D., Caserini, E., Bersanelli, M., Cappellini, B., & Mennella, A. 2003, A&A, 410, 847
- Reich, P., & Reich, W. 1986, A&AS, 63, 205
- Roger, R. S., Costain, C. H., Landecker, T. L., & Swerdlyk, C. M. 1999, A&AS, 137, 7
- Salvaterra, R., & Burigana, C. 2002, MNRAS, 336, 592
- Sironi, G., Boella, G., Bonelli, G., Gervasi, M., Vaccari, A., & Zannoni, M. 1999, in AIP Conf. Proc. 476, 3K Cosmology, ed. L. Maiani, F. Melchiorri, & N. Vittorio (Woodbury: AIP), 149
- Sironi, G., Bonelli, G., & Limon, M. 1991, ApJ, 378, 550
- Sironi, G., Limon, M., Marcellino, G., Bonelli, G., Bersanelli, M., Conti, G., & Reif, K. 1990, ApJ, 357, 301
- Smoot, G. F., et al. 1985, ApJ, 291, L23
- Stankevich, K. S., Wielebinski, R., & Wilson, W. E. 1970, Australian J. Phys., 23, 529
- Tartari, A., Zannoni, M., Gervasi, M., Boella, G., & Sironi, G. 2008, ApJ, 688, 32 (Paper III)
- Wolleben, M., Landecker, T. L., Reich, W., & Wielebinski, R. 2006, A&A, 448, 411
- Zannoni, M., et al. 1999, in AIP Conf. Proc. 476, 3K Cosmology, ed. L. Maiani, F. Melchiorri, & N. Vittorio (Woodbury: AIP), 165